Non-Equilibrium Fractionation Factors for D/H and $^{18}O/^{16}O$ During Oceanic Evaporation in the North-West Atlantic Region

D. Zannoni[1], H. C. Steen-Larsen[1], A. J. Peters[2], S. Wahl[1], H. Sodemann[1] and A. E. Sveinbjörnsdóttir[3]

[1]Geophysical Institute, University of Bergen and Bjerknes Centre for Climate Research, 5007, Bergen, NORWAY.
[2]Bermuda Institute of Ocean Sciences, St. George's GE01, BERMUDA.
[3]Institute of Earth Sciences, University of Iceland, Reykjavik, ICELAND.

Corresponding author: Daniele Zannoni (daniele.zannoni@uib.no)

Key Points:

- Observation-based non-equilibrium fractionation factors for water isotopologues during ocean evaporation are proposed.
- Significant correlation observed between non-equilibrium fractionation factors and 10-m wind speed.
- No evidence of distinction is found between smooth and rough regimes for isotopic fractionation during ocean evaporation.

Abstract

Ocean isotopic evaporation models, such as the Craig-Gordon model, rely on the description of non-equilibrium fractionation factors that are, in general, poorly constrained. To date, only a few gradient-diffusion type measurements have been performed in ocean settings to test the validity of the commonly used parametrization of non-equilibrium isotopic fractionation during ocean evaporation. In this work we present six months of water vapor isotopic observations collected from a meteorological tower located in the northwest Atlantic Ocean (Bermuda) with the objective of estimating non-equilibrium fractionation factors (k, ‰) for ocean evaporation and their wind speed dependency. The Keeling plot method and Craig-Gordon model combination was sensitive enough to resolve non-equilibrium fractionation factors during evaporation resulting into mean values of k_{18}= 5.2±0.6 ‰ and k_2= 4.3±3.4 ‰. Furthermore, we evaluate the relationship between k and 10-m wind speed over the ocean. Such a relationship is expected from current evaporation theory and from laboratory experiments made in the 1970s, but observational evidence is lacking. We show that (i) in the observed wind speed range [0 – 10 m s^{-1}] the sensitivity of k to wind speed is small, in the order of -0.2 ‰ $m^{-1}s$ for k_{18}, and (ii) there is no empirical evidence for the presence of a discontinuity between smooth and rough wind speed regime during isotopic fractionation, as proposed in earlier studies. The water vapor d-excess variability predicted under the closure assumption using the k values estimated in this study is in agreement with observations over the Atlantic Ocean.

Plain Language Summary

Phase changes between liquid and vapor continuously occur in the atmospheric water cycle. These phase changes affect the isotopic composition of water through an effect called isotopic fractionation. Depending on the thermodynamic conditions, two types of isotopic fractionation exist: equilibrium and non-equilibrium fractionation. While equilibrium fractionation is relatively well constrained by theoretical considerations from statistical mechanics and laboratory tests, non-equilibrium fractionation is less well constrained theoretically and needs to be investigated by empirical methods. Ocean evaporation is a non-equilibrium process and still today there is little agreement on which are the best non-equilibrium fractionation factors to use in evaporation models. Currently, non-equilibrium fractionation factors are calculated following a parametrization based on wind speed from wind tunnel experiments performed in the 1970s. The reported wind effect has never been directly observed over the ocean. In this study we report non-equilibrium fractionation factors for ocean evaporation estimated directly by measuring water vapor isotopic composition at two heights in an oceanic condition and explore their relationship with wind speed. Since having accurate fractionation factors is fundamental when using stable isotopes to model the Earth's water cycle, the results of this study can help improving the performance of numerical models when describing ocean evaporation.

1 Introduction

Stable isotopes of hydrogen and oxygen in water have been used successfully for more than 50 years to study processes of the Earth's water cycle. Specifically, using water stable isotopes allows atmospheric processes of the water cycle to be studied on time scales spanning the scale of turbulent eddies to glacial-interglacial time scales (Galewsky et al., 2016). Modulation of the water vapor isotopic composition, hereafter in delta notation, is linked to several physical processes occurring in the atmosphere involving phase change and turbulent mixing. On the one hand, isotope ratios of $^{18}O/^{16}O$ ($\delta^{18}O$) and D/H (δD) in precipitation are

largely controlled by upstream precipitation during moisture transport and isotopic equilibrium effect during phase changes (Craig, 1961; Dansgaard, 1964; Rozanski et al., 1993). So-called temperature and continental effects visible on isotopic composition of precipitation are also visible on tropospheric water vapor (Galewsky et al., 2016). On the other hand, the deviation from the linear relationship between $\delta^{18}O$ and δD (i.e., d-excess=$\delta D-8*\delta^{18}O$) in precipitation is controlled by non-equilibrium effects linked to evaporative conditions of moisture source areas (Craig & Gordon, 1965; Merlivat & Jouzel, 1979), by moisture recycling above the continents (Risi et al., 2013), as well as by sub-cloud droplet evaporation (Stewart, 1975) and cloud microphysics (Ciais & Jouzel, 1994). The d-excess signal in surface water vapor at daily and sub-daily time scale has been shown to be largely affected by local surface fluxes, advection and exchange with the free atmosphere both over land (e.g. Aemisegger et al., 2014) and over the ocean (e.g. Benetti et al., 2014).

1.1 Magnitude and control of non-equilibrium fractionation during ocean evaporation: objectives of the study

Isotopic fractionation can occur under two different conditions during water phase change in the hydrological cycle: equilibrium and non-equilibrium. While isotopic fractionation effects under equilibrium conditions above 0°C are well understood, non-equilibrium fractionation effects are still poorly constrained. During evaporation, a non-equilibrium process, the relative weight of molecular and turbulent diffusion controls the magnitude of non-equilibrium fractionation. The molecular diffusivity ratios for $HD^{16}O/H_2{}^{16}O$ and $H_2{}^{18}O/H_2{}^{16}O$ in air are 0.9757 and 0.9727 (Merlivat, 1978). However, these need to be scaled in evaporation models because evaporation in an oceanic environment is not a pure molecular diffusion-controlled process but also include a turbulence component, that is not fractionating (Brutsaert, 1965, 1975, Craig & Gordon, 1965). To account for this turbulent component, a parametrization of non-equilibrium fractionation factors dependent on wind speed as the only independent variable has been proposed (Merlivat & Coantic, 1975). This parametrization, together with relative humidity (RH) and sea surface temperature (SST), was further used in Merlivat and Jouzel (1979) to model the variability of water vapor d-excess under a global closure assumption (i.e. of a closed water budget). However, several recent studies have questioned the assumed role of SST and wind speed on the controls of non-equilibrium fractionation based on water vapor d-excess observations (Bonne et al., 2019; Steen-Larsen et al., 2014; Pfahl and Wernli, 2008; Pfahl and Sodemann, 2014; Steen-Larsen et al., 2015; Uemura et al., 2008). Other studies argued that water vapor d-excess above the ocean surface may not be influenced solely by ocean surface evaporative conditions, namely RH and SST, but also by the coupling between the Marine Boundary Layer (MBL) and the free troposphere (Benetti et al., 2018; Galewsky et al., 2022) as well as by air–sea interactions during cold and warm advection (Thurnherr et al., 2021). Consequently, it can be concluded that a substantial uncertainty exists on the magnitude of non-equilibrium fractionation during evaporation in real-environmental conditions and, still, no agreement exists on the controls of non-equilibrium fractionation by SST and wind speed (e.g. Gonfiantini et al., 2020). This lack of consensus drives the following questions: which non-equilibrium fractionation factors are the most accurate to use during the evaporation process in the MBL? Is there empirical evidence for a dependency between non-equilibrium effects and wind speed in the oceanic environment? If a relationship between wind speed and non-equilibrium fractionation exists, is it captured by the established parametrizations by Merlivat

and Jouzel (1979) which are based on wind tunnel experiments? These research questions will be addressed in this study by:

1. Estimating the non-equilibrium fractionation factors for $\delta^{18}O$ and δD that best-fit the observed isotopic composition of the evaporation flux from the ocean surface.
2. Test the validity of theoretical parametrization of the wind speed effect on non-equilibrium fractionation with observations of the isotopic composition of the evaporation flux over the ocean.

The impacts and limitations of the method applied for estimating the non-equilibrium fractionation factors and the isotopic composition of evaporation flux from the ocean surface will be discussed in detail, focusing on potential SST and ocean isotopic composition inhomogeneities in the study area. Furthermore, we will discuss the sensitivity of the linear relationship between d-excess and RH normalized to SST (h_s) under the closure assumption (hereafter, CA) by using the non-equilibrium fractionation factors estimated in this study and other available datasets of water vapor observations in the MBL.

1.2 Estimating the isotopic composition of the evaporation flux using near-surface water vapor observations

The isotopic composition of the evaporation flux can be estimated by three micrometeorological methods: Eddy Covariance (Braden-Behrens et al. 2019, Wahl et al. 2021), Flux Gradient (FG, Yakir and Wang 1996) and Keeling Plot (KP, Keeling, 1958). The Eddy Covariance method requires high-frequency measurements of wind speed and vapor isotopic composition that are difficult to obtain but provides direct observations of the isotopic composition of the evaporation flux. FG and KP methods do not require high-frequency measurements but rely on assumptions of the environmental conditions during evaporation. In principle, FG and KP can be used to estimate the isotopic composition of the evaporation flux by direct application of a fully turbulent mixing model between two end members: a constant water vapor flux and a background moisture of constant isotopic composition (binary mixing model). In this context, the application of KP and FG methods would be best addressed in an oceanic environment, where the main source of evaporating water is the ocean surface. Keeping the closure assumption valid from a local point of view, i.e. assuming that all the water vapor in the MBL originates from the evaporation flux, single level near-surface observations of the water vapor d-excess should be representative of local evaporative conditions, namely SST, RH and wind speed. This assumption, however, is no longer valid when measurements are performed in low evaporation areas or for periods when other prevailing water vapor exchange processes, such as advection and/or entrainment, occur in the atmosphere. The expected wind speed effect could be smoothed out in the vapor d-excess signal by other processes and observations of water vapor isotopic composition at a single height level then might not be representative of the evaporation flux. Furthermore, variability of the water vapor isotopic composition in the free atmosphere, during advection and via contribution of sea-spray evaporation can introduce errors in the estimation of the isotopic composition of the flux. Therefore, observations at different height levels should be used to estimate the isotopic composition of the evaporation flux with KP and FG instead of single height time series of water vapor isotopic composition. Many profile measurements are available in continental settings from atmospheric research and flux towers (e.g. Griffis et al., 2016) but are scarce over the ocean. Most of the available profile observations

over the ocean were acquired over short time frames with cryotrapping (Gat et al., 2003; Craig & Gordon, 1965). More recently, two-heights profiles were obtained during research cruises but some additional uncertainties were introduced due to the use of different instruments for isotopic analysis at each height, ship movement, ship exhaust, and ocean spray contribution to the vapor composition (Thurnherr et al., 2020). In this study we analyze a unique six months (20th June to 30th December 2013) data set of continuous observations of water vapor isotopic composition sampled at two heights from a meteorological tower located in the northwest Atlantic region (Bermuda, Figure 1) and use it to estimate the isotopic composition of the ocean evaporation flux.

[FIGURE 1]

Given that Bermuda is located in part of the source region for the precipitation which is deposited in Greenland, this study is also relevant for ice core science (Johnsen et al., 1989; H. Sodemann et al., 2008), questioning the type of information deduced from d-excess in paleoclimate archives on the evaporative conditions at the source regions such as the role of wind speed and SST (e.g. Jouzel et al., 2007; Steen-Larsen et al., 2011, Markle et al., 2018 Osman et al., 2021).

2 Materials and Methods

2.1 Study site

The study site is located in the south-western part of Bermuda, at the Tudor Hill Marine Atmospheric Observatory (THMAO) operated by Bermuda Institute of Ocean Sciences (32.26° N 64.88° W). The THMAO tower faces the coast (distance ~30m) and is 20.5 m high. Considering the altitude of the tower base (~29 m AMSL), the top of the tower faces the ocean at a height of ~50 m AMSL. The climatic conditions at Bermuda are characterized by a humid subtropical climate, strongly affected by the Gulf Stream. The study area is situated in the so-called Bermuda-Azores High, a large subtropical center of high atmospheric pressure. The high-pressure system is primarily centered near the Bermuda Islands during summer and fall, and near Azores during winter and early spring. Ocean evaporation around Bermuda Island is strong due to its location near the Gulf Stream area and due to cold air advection, especially during the winter (Aemisegger & Papritz 2018). ERA5 reanalysis data (Hersbach et al., 2020) shows that the evaporation flux (E) in the study area exceeds the precipitation flux (P), as expected (P-E = -1.34 mm day^{-1}). Analysis with a Lagrangian moisture source diagnostic (Läderach and Sodemann, 2016) for the Jun-Dec 2013 observation period calculated with ERA-Interim reanalysis data (Dee et al., 2011) at a 1˚x1˚ resolution and a 6h time step revealed that 45% of lower tropospheric moisture originated in a 10˚x10˚ area around the study site (inset map in Figure 1). The evaporation flux footprint was also evaluated with a flux footprint model (Kljun et al., 2015), suggesting that 90% of the fetch area at the top of THMAO is within 2800 m. Due to its position and climatic conditions, the island of Bermuda is therefore an ideal study site for evaporation-related processes and their control on the d-excess signal because ocean evaporation is the dominant source of the MBL vapor and there is low influence of continental water vapor.

2.2 Meteorological and ocean observations

Air temperature, relative humidity (T, RH, Campbell Scientific EE181-L125-PT), wind speed and wind direction (WS, WD, R.M. Young CAT NO. 05103) were measured at the top inlet (50 m AMSL) of THMAO. The wind speed measured at 50 m AMSL was corrected to 10 m AMSL

assuming a log-law wind profile and a roughness length of 0.2 mm (Stull, 1997). Sea Level Pressure (SLP) and precipitation (P) were measured ~20 km northeast at the L. F. Wade International Airport (TXKF) by the Bermuda Weather Service. MBL height data was retrieved from ERA5 global reanalysis data (blh variable), which is based on a critical value of the bulk Richardson number and depends on the vertical wind shear and buoyancy (ECMWF, 2017). Gridded blh was retrieved at 0.25°x0.25° and 1-hour temporal resolution and was linearly interpolated to the study site location.

2.3 SST and Ocean water isotopic composition

Salinity and SST observations are available from buoys inside the reef at 3h time resolution (Hog Reef and Crescent Reef), at St. George Harbor at daily resolution, and outside the reef at monthly resolution for the Bermuda Atlantic Time-series Study (BIOS, 2021). Salinity and SST measurement locations are reported in Figure 1. To minimize potential bias due to local SST variations we chose the averaged Operational Sea Surface Temperature and Sea Ice Analysis (OSTIA, UK MET OFFICE, 2005) data as representative for SST of the study site. High correlation is observed between average SST measured inside the reef and OSTIA product averaged on a 1˚x1˚ box centered on Bermuda (R Pearson> 0.96) but better agreement, in terms of maximum absolute difference, was observed between BATS and OSTIA data (1.08 ˚C) than for Crescent reef and OSTIA data (2.55 ºC).

No measurements of ocean water isotopic composition near the study site are available for the period of interest, but the temporal variability of the ocean isotopic composition in the study area is assumed to be very low. Several sources have been evaluated for estimating the most representative composition of ocean water around the study site: gridded dataset (LeGrande & Schmidt, 2006), North Atlantic cruises published data (Benetti et al., 2014, 2017a) as well as from samples collected at the BATS site two years before this campaign (BIOS, 2021). The isotopic composition of the ocean in this study is assumed to be $\delta^{18}O_L$ = 1.09‰ and δD_L = 7.25‰, which is the average between the isotopic composition calculated with the salinity to isotope conversion (Benetti et al., 2017a) applied to local salinity data (BIOS, 2021) and the ocean isotopic composition estimated from gridded dataset (LeGrande & Schmidt, 2006). Full details on ocean water isotopic composition are reported in Supporting Info, Text S1.

2.4 Water vapor isotopic composition and humidity observations

Ambient air was sampled at THMAO tower at two different heights: 2.5 m and 50 m AMSL. Ambient air was continuously pumped from the two inlets to a manifold located at the tower base that was connected to a Picarro L2120-i isotopic water vapor Cavity Ring-Down Spectroscopy (CRDS) analyzer. Quick air transport was ensured through heated copper tubing using a 10 L min^{-1} sampling pump. The sampling line was switched between the two inlets every 15 minutes and when one inlet was connected to the analyzer, the other inlet was flushed by a secondary 5 l min^{-1} pump. This configuration ensured a continuous circulation of air inside the tubing system, thus minimizing the lag and memory effect for the two inlets. The CRDS analyzer sampled water vapor from the main line at its nominal flow rate (~40 sccm min^{-1}) and recorded humidity and water isotopic composition at ~0.56 Hz frequency. To reduce the memory effect due to the switching between top and bottom inlet, the first 10 minutes of data after valve switching was removed and the last 5 minutes was averaged. In this way, the 5 minutes average is assumed to be representative of the isotopic composition during measurement for each level, which yields one measurement point per half hour per level. The inlet can be approximated to a

first-order low pass filter with transfer function $H=1/(\tau+1)$, where τ is the time the system's response need to reach 63% of the final value for a step change from zero initial condition ($\tau(\delta^{18}O)$ = 212 s, $\tau(\delta D)$ = 310s). Assuming the final value of the signal to be 1 for a normalized step change, we estimated that the magnitude (mag) of signal attenuation is only -1.9 dB for $\delta^{18}O$ and -3.4 dB for δD ($dB = 20\log_{10}(mag)$) and the phase difference between $\delta^{18}O$ and δD signal is <9˚ with an averaging window of 0.5 hours. The error introduced by signal attenuation and phase difference between $\delta^{18}O$ and δD signal in the system is considered insignificant at the time resolution used in this study. However, a small persistent bias in d-excess can still be present during monotonically variations of $\delta^{18}O$ and δD signals.

The isotope readings of the water vapor analyzer were calibrated on the VSMOW-SLAP scale (IAEA, 2009) using several laboratory standards at the beginning and towards the end of the observation period. Drift-correction measurements were carried out on a sub-daily basis (every 6-12 hours) and humidity-isotope response curves were performed every 1-2 months during the study period to correct for the humidity dependency of water vapor isotopic composition. Precision of water vapor isotopic measurement are expected to be 0.14‰ for $\delta^{18}O$ and 1.1‰ for δD. The reader is referred to a previous study conducted at THMAO for additional details on the setup of the sensing system, on the calibration protocol and on sensing system performances (Steen-Larsen et al., 2014). Humidity observations of the CRDS analyzer (moist mixing ratio, w [ppmv]) were calibrated against RH observations at the top inlet.

2.5 Estimation of the evaporation flux isotopic composition

The isotopic water vapor observations acquired with the CRDS analyzer represent the time-averaged atmospheric moisture composition at a certain height above sea level. We used the KP method between the two inlets to estimate the isotopic composition of the water vapor flux (δ_E). In the KP method, δ_E is assumed to be equal to the intercept of the linear best-fit model between the isotopic composition of water vapor ($\delta^{18}O$ or δD) and the inverse of humidity (1/w) at the two different height levels. The uncertainties for δ_E ($\sigma_{\delta E}$) were calculated as a function of instrument precision, sample size, and atmospheric conditions (Good et al., 2012). However, in our case the number of observations for each time-step is equal to the degrees of freedom required to calculate the uncertainty associated with the flux composition. Therefore, observations were grouped on a daily basis and the error on flux composition was calculated when more than two observations were available. It is important to note that the computation of the flux composition with the KP method is valid only under the following assumptions:

1. The mixing process in the gradient measurement space is fully turbulent and does not introduce any fractionation: turbulent diffusion is the same for all isotopologues.
2. Water vapor flux is constant with height: the mixing ratio and water vapor isotopic composition vertical profiles is characterized by a monotonic trend.
3. Variability of water vapor isotopic signal is not significantly affected by advection or entrainment from the free troposphere during the acquisition of water vapor profiles.
4. Isotopic composition of source water is constant in the time interval considered.

Therefore, water vapor observations were filtered to fulfill the above mentioned assumptions, as further discussed in Section 3.2 and Section 5.1. It is worth noting that the regression method used to calculate the isotopic composition of the evaporation flux can also impact the result, as recently shown in Hu et al. (2021). In this study we used the ordinary least squares method to evaluate the KP intercept. According to Hu et al. (2021), the ordinary least squares method is

more robust than e.g. the Geometric Mean Regression method and should be comparable with the York Solution method under large fetch conditions. In this context, the isotopic composition of water vapor measured at the top inlet is assumed to be representative of water vapor in the MBL with a fetch area similar to the one estimated with the moisture diagnostic. However, because the large height difference between the bottom and top inlets results into different fetch areas, the water vapor isotopic composition at the bottom inlet was corrected ($\delta^{18}O$=+0.07‰ and δD=+0.75‰) accounting for the SST difference between open ocean SST and reef area SST, as further discussed in Section 5.2.

2.6 Estimation of non-equilibrium fractionation factors

The Craig-Gordon (CG) (Craig & Gordon, 1965) model was used to calculate δ_E (‰) from the ocean surface following the notation introduced in Merlivat and Jouzel (1979), as reported in equation (1):

$$\delta_E = (1-k)\frac{\alpha_{V/L}(1+\delta_L)-h_s(1+\delta_A)}{(1-h_s)} - 1 \qquad (1)$$

where $\alpha_{V/L}$ [<1] is the equilibrium fractionation factor between vapor and liquid (Horita & Wesolowski, 1994), h_s [1] is the RH measured at the top of the turbulently mixed sublayer relative to ocean surface temperature (OSTIA SST [K], averaged on a 1˚x1˚ box centered on Bermuda), k [1] is the non-equilibrium fractionation factor, δ_A is the isotopic composition of atmospheric moisture [1], δ_L is the isotopic composition of the ocean water [1]. The non-equilibrium fractionation factor k (reported in ‰ hereafter) is estimated from a direct comparison between the observed (KP) and modeled (CG) isotopic composition of the evaporation flux. For a given flux observation i, it is possible to calculate m different values of the flux composition with the CG model by varying the non-equilibrium fractionation factors within a certain range. The best k values are then calculated by error minimization between the modeled and observed evaporation flux composition for each pair of top and bottom inlet observations in the filtered dataset. To estimate the average values of k, the inverse of the errors of the observed flux composition were used as the weights in the computation of the average. Populations of mean non-equilibrium fractionation factors k were estimated with bootstrapping, repeating the above sequence for 10^4 times with random resampling. Additional details on how the non-equilibrium fractionation factors are calculated are reported in Supporting Info, Text S2 and Text S3.

3 Data description

3.1 Dataset

Time series of water vapor at the top and bottom inlets were resampled using a common UTC time indexing with a resolution of 30 minutes through linear interpolation. Meteorological observations were also averaged and synchronized accordingly to CRDS observations. The water vapor time series used in this study includes 8793 datapoints, representative of 30-minutes averaged observations of water vapor isotopic composition at two height levels over the ocean surface. The complete dataset accounts for 95% coverage of the study period (Figure 2).

[Figure 2]

Based on d-excess, the pattern of atmospheric water vapor composition can be divided into two main groups: a first group from summer to mid-autumn with gentle daily to weekly d-excess oscillations and a second group, from mid-autumn to early winter, with larger and more pronounced d-excess oscillations at weekly scale. The transition in the d-excess pattern follows the general decrease in humidity and the large h_s variability observed from late October (marked by gray triangles in Figure 2). The temperatures decrease in autumn-winter is also linked to a small shift of the center of mass of moisture sources toward the north-west (not shown). This shift can be linked to the increase in baroclinicity towards autumn and winter and to the more frequent passage of extratropical cyclones over the gulf stream leading to strong ocean evaporation (Aemisegger & Sjolte, 2018).

3.2 Filtered dataset for flux estimation

To guarantee high data quality and for maximizing the validity of assumptions under KP (Section 2.5, points 1 - 4), several constraints were introduced to filter the dataset. The rationale behind those constraints is summarized for each variable in Table 1. By means of the quality control filtering criteria, the sample size is reduced from 8793 to 814 30-minutes averaged observations (~10% of available data). The variables that are most responsible for the exclusion of data points are the daytime and the western wind sector constraints. Just those two filtering criteria account for approximately 85% of rejections. However, these strict filtering criteria were necessary because of the local evapotranspiration signal contribution, with wind blowing from inland and dew formation caused by night cooling. The remaining filtering criteria accounted for an additional 5% of rejections.

Most of the observations (~90%) of the filtered dataset were selected between 20th June and 23rd October, as shown in Figure 2. From the perspective of data representativeness, the main features of the dataset after the filtering procedure are: (i) slightly changed mean and median values (for $\delta^{18}O$ and d-excess) and reduction of secondary modes in d-excess distribution; (ii) statistically significant change in regression parameters for d-excess vs h_s; (iii) significant reduction of observations characterized by deeper MBL (blh > 1000 m, from 17% to 4%); (iv) change of the wind speed distribution in terms of the mean (from 2.8 ms^{-1} to 4.0 ms^{-1}). Therefore, the main consequences of data reduction are a larger impact of shallow atmospheric mixing, a smaller influence of large MBL development and less periods characterized by low wind speed conditions. More details on the impact of data filtering on the distribution shape of variables of interest are reported in Supporting Info, Text S4.

4 Results

4.1 The isotopic composition of the evaporation flux (δ_E) from the ocean surface

Descriptive statistics of the evaporation flux isotopic composition from the ocean surface and the water vapor isotopic composition observed at the top inlet during daytime are reported in Table 2. On average, the number of data points available for KP calculation is 20 per day and the coefficients of determination for both $\delta^{18}O$ and δD regression lines are high ($R^2 = 0.78$, on average). For comparison, the Flux Gradient method (FG, Lee et al., 2007) was also used to compute the isotopic composition of evaporation flux, obtaining nearly identical results but different uncertainties, especially for δD ($\sigma_{\delta E}$ = 0.59‰ and 51‰ for $\delta^{18}O$ and δD, respectively).

The high similarity between the FG and KP methods is consistent with other studies (Good et al., 2012; Hu et al., 2021) which is why we focused on the KP method. As expected, the isotopic composition of the flux is enriched with respect to the atmospheric water vapor composition and depleted compared to the ocean isotopic composition. The mean δD of the evaporation flux is between recent estimates of the global mean HDO fluxes (-37.6‰ following Good et al., 2015) and estimates made in past studies (-22‰ following e.g. Gat, 1996). No evident trend was observed for daily δ_E during the study period, for both $\delta^{18}O$ and δD (Supporting Info, Figure S6).

4.2 Non-equilibrium fractionation factor distributions estimated with flux observations

Non-equilibrium fractionation factors are expressed hereafter in term of k_{18} (for $\delta^{18}O$) and k_2 (for δD) to allow a direct comparison with the parametrization proposed in Merlivat and Jouzel (1979). Applying the bootstrapping method (10^4 samples with 80 observations in each) to the filtered dataset yields a mean ± 1 std. dev. k_{18} = 5.21 ± 0.64‰ and k_2 = 4.32 ± 3.41‰, as show in Figure 3.

[Figure 3]

The obtained *k* PDFs are in the range predicted by the parametrization proposed in Merlivat and Jouzel (1979). For k_{18}, the distribution of the mean values falls in the middle of the parametrizations for the smooth and rough wind speed regimes as proposed by Merlivat and Jouzel. A similar result was obtained for the average k_2, the PDF of which is however characterized by a significantly larger spread. Consistent with previous works, non-equilibrium fractionation factors are on average ~0.20 - 0.25 times the value expected for a purely diffusivity-driven evaporation process (Merlivat, 1978). For reference, the *k* values estimated in other studies are also reported in Figure 3 (Pfahl & Wernli, 2009; Uemura et al., 2010). Note that the k_{18} values estimated in this study are 2-3 ‰ smaller than previous studies and more consistent with the parametrization of k_{18} proposed in Merlivat and Jouzel (1979). On average the ratio k_2/k_{18} is equal to 0.83, similar to 0.88 in Merlivat and Jouzel (1979) and 0.84 reported in Luz et al. (2009).

4.3 Observed relationship between non-equilibrium fractionation factors and 10-m wind speed

To test a dependency of the fractionation factors *k* on wind speed, the filtered dataset was binned in 10-m wind speed classes with bin size 0.5 m s^{-1}. For each wind speed class, the non-equilibrium fractionation factors were calculated using the KP method at 30 min time step. Afterwards, mean and standard error of *k* were calculated for each wind speed bin center. Mean k_{18} values obtained in such way are reported as a function of 10-m wind speed in Figure 4.a.

[Figure 4]

In the wind speed range [0.5 – 10] m s^{-1} the negative correlation between k_{18} and wind speed is high and statistically significant (r=-0.72, p-value=$1x10^{-3}$). The parametrization proposed in Merlivat and Jouzel (1979) agrees well with the observed k_{18} variability between 0.5 and 6 m s^{-1}, with an average absolute difference of 0.1‰. Most importantly, the differences between parametrized and observed k_{18} values are normally distributed around zero (Kolmogorov-Smirnov and Shapiro-Wilk p-values equals to 0.13 and 0.34, respectively) and the errors can therefore be attributed to random noise in the measurement. On the other hand, observed k_{18} are 2‰ larger than modeled k_{18} for rough regime parametrization between 6 and 10 m s^{-1}. Moreover, the theoretical

wide discontinuity between smooth and rough regime expected at ~6 m s^{-1} is not visible in the observations. A decrease of k_{18} in the 7 ± 1 m s^{-1} wind speed region is noticeable but k_{18} observations quickly approach the main decreasing trend. The observed k_{18} values are on average 1.7‰ higher than the ones calculated with the rough regime parametrization between 7 and 10 m s^{-1}. Despite the small number of observations at wind speed above 7 m s^{-1}, this study: (i) does not provide sufficient experimental evidence that there are two different regimes in the wind dependency of k_{18}; and (ii) suggests that a continuous decrease of k_{18} as a function of wind speed is more likely in the interval [0.5 – 10] m s^{-1}. Such a decrease can be approximated by the following simplified equation:

$$k_{18} = (-0.16 \pm 0.04) * WS + (6.6 \pm 0.3)\ ‰ \qquad (2)$$

where WS is the 10-m wind speed in m s^{-1}. Equation (2) highlights that in the wind speed range [0.5 – 10] m s^{-1} the sensitivity of k_{18} to wind speed is only -0.16 ± 0.04 ‰ $m^{-1}s$. Data filtering prevents to calculate k_{18} at lower wind speed values, mainly because of the thresholds on humidity and isotopic composition differences between the two inlets. When such thresholds are removed, the number of observations increases on the left side of the wind speed distribution (Figure 4.c), with a ~5% increase of the sample size but yields a larger uncertainty for the lowest wind speed bin (SE=1.7‰, not shown). The impact of the presence/absence of humidity and isotopic composition difference thresholds between the two inlets is minimal in the k_{18} wind speed relationship. Indeed, the average absolute difference of k_{18} with/without those thresholds is only 0.1‰ in the [0.5 – 10] m s^{-1} wind speed range, with a minimal increase of the slope of 0.04‰ $m^{-1}s$. Unfortunately, the limited number of datapoints above 10 m s^{-1} does not allow any other speculation on the dependency of k_{18} to higher wind speed and prevents a better constraining of the rough regime. Furthermore, it is possible that other processes such as sea spray contribution might start to become important in the net evaporation flux at higher wind speeds (Andreas et al., 1995; Veron, 2015). Therefore, equation (2) must be considered valid only in the [0.5 – 10] m s^{-1} wind speed range.

Continuing with k_2, observations are scattered and very noisy on the k_2 vs wind speed coordinate plane (data reported in Supporting Info, Figure S5) because δD is less strongly influenced by non-equilibrium fractionation than $\delta^{18}O$. The correlation between k_2 and wind speed is low and not significant within the [0.5 – 10] m s^{-1} wind speed range (r=-0.34, p-value=0.15). Observations are not in agreement with Merlivat and Jouzel (1979) parametrization, neither for the smooth nor for the rough regime, with an average absolute difference of 1.4‰ from the model. The noise in k_2 observations drastically affects the variability of the k_2/k_{18} ratio, which shows an average value of 0.8 and a standard error of 0.1 (Figure 4.b). It is worth noting that the k_2/k_{18} ratio is not correlated with 10-m wind speed.

5. Discussion

5.1. Method sensitivity to filtering criteria

The KP method is based on assumptions that might partly be violated in a dynamic oceanic environment. Even on an island in the middle of the ocean, variability of local evaporation sources due to e.g. vegetation and change in wind direction, can affect the validity of a simplified

binary mixing model, with ocean and free atmosphere as the only end members. The strict filtering criteria used in this study to estimate the isotopic composition of the evaporation flux and the non-equilibrium fractionation factors tries to select the data for maximizing the validity of the assumptions behind an ideal binary mixing model. This strict filtering, however, reduced the original dataset size significantly, as mentioned before. Here we discuss how each filtering criteria affects the results shown in Section 4.1 - 4.3, removing only data that is affected by moisture input from precipitation events (Figure 5).

[Figure 5]

When all the filters are switched off, the isotopic composition of the evaporation flux decreases significantly and the mean δ_E values are not in accordance what would be expected for evaporation from the ocean (Gat, 1996; Good et al., 2015; Craig & Gordon, 1965), as shown in Figure 5.a and b. Both daytime and western wind sector filters enrich the isotopic composition of the flux. However, westward wind direction has the largest impact on $\delta^{18}O$ flux while daytime and westward wind direction filtering contributes likewise on δD flux. This different impact for $\delta^{18}O$ and δD fluxes highlights the different sensitivity of the method to environmental changes in daytime-nighttime temperatures (larger effect on δD, minimal on $\delta^{18}O$) and on water vapor sources (ocean source vs local evapotranspiration, similar effect for both δD and $\delta^{18}O$). The lower night temperatures, coupled to the poor ventilation due to low wind speeds during the night, increase RH substantially. Such stable conditions might promote the contribution of transpiration signal from local vegetation on the moisture near the ground. The k values show the mirror image of the evaporation flux composition. Indeed, wind direction filtering contributes the most on decreasing k_{18} value while time and wind direction contribute nearly equally to decreasing k_2. Enabling/removing the thresholds on isotopic and humidity differences between the two inlets have only a marginal impact on the average flux composition and k estimation.

5.2 Impact of ocean surface composition and SST inhomogeneity in the fetch area on *k* estimation

The top and bottom inlets are sensitive to different fetch areas because of the height difference between the two inlets at THMAO (~48 m). The flux footprint prediction model (Kljun et al., 2015) suggested that 90% of the fetch area for the bottom inlet is within 100 m while for the top inlet is within 2800 m. The island of Bermuda is characterized by shallow waters close to the coast. Therefore, it is possible that local circulation of ocean water within the coral reef system can have an impact on SST variability and on surface water isotopic composition. Continuous measurement of SST and ocean isotopic composition covering the whole study area are not available. However, a first approximation of the variability of SST and salinity (as a proxy of evaporation) in the study area can be retrieved from buoys and BATS data, as shown in Figure 6.a and Figure 6.c. In this context, the variability of SST can be used to estimate the equilibrium water vapor variability in the study area (Figure 6.b) while the variability of salinity can be used to estimate the variability of ocean composition by applying the salinity to isotope conversion following Benetti et al (2017a) (Figure 6.d).

[Figure 6]

It is reasonable to assume that OSTIA SST is more representative of the isotopic composition of equilibrium water vapor for the top inlet while the SST measured near the island coastline is

representative for the bottom inlet. To account for the different fetch areas, we correct the water vapor isotopic composition at the bottom inlet by adding the mean deviation of St. George equilibrium SST from OSTIA, that is +0.07‰ and +0.75‰ for $\delta^{18}O$ and δD, respectively (i.e. the mean of blue PDF in Figure 6.b). As anticipated in Section 2.5, we used this correction to calculate the isotopic composition of evaporation fluxes shown in this study. Similarly, the ocean composition within the reef is likely more representative of evaporating water within the reef, hence, an approximate offset can be added to the isotopic composition of the ocean equal to -0.06‰ and -0.38‰ for $\delta^{18}O$ and δD, respectively (i.e. the mean of the green PDF in Figure 6.d). Next, we discuss how large is the impact of such corrections on the estimation of the k values and on the relationship between k and wind speed. As shown in Table 3, the inhomogeneity of ocean composition can introduce a bias in k_{18} and k_2 in the order of 0.3‰ and 1.3‰, respectively. These biases, are smaller than the uncertainties of k_{18} and k_2. On the other hand, SST inhomogeneity in the study area can introduce a 0.8‰ and 8‰ bias in k_{18} and k_2 estimation. When the SST correction is implemented, the k_{18} bias is still comparable to k_{18} uncertainty while k_2 differs significantly when the offset is introduced (66% absolute deviation). Therefore, SST has a larger impact on δD than on $\delta^{18}O$ and the impact of ocean composition inhomogeneity in the study area is lower than the impact of SST in the estimation of k_{18} and k_2. It should be noted that neither the correction for SST nor the correction for ocean composition take into account the magnitude of the evaporation flux in the estimation of the average δ_E. The average δ_E should be in principle weighted by mass flux from the ocean surface. However, similar non-equilibrium fractionation factors were obtained with an SST correction based on the day-by-day difference between OSTIA and St. George SST instead of the mean difference during the whole study period (5.37 and 5.16 for k_{18} and k_2, respectively). A key point is that SST correction and Salinity + SST corrections lower the k_2/k_{18} ratio below unity (0.83 and 0.57), which makes sense from the physical point of view, since the ($1-HD^{16}O/H_2{}^{16}O$) quantity needs to be smaller than ($1-H_2{}^{18}O/H_2{}^{16}O$) (e.g. as recently shown in Hellmann & Harvey, 2020). However, when both salinity and SST corrections are implemented, k_2 is too low and not consistent, e.g. with recent water vapor observations in the Atlantic Ocean (Bonne et al., 2019). Finally, both corrections do not significantly affect the observed correlation between k_{18} and wind speed. The main effect of the corrections on k_{18} and k_2 leads to shifts in the distributions without changing their shapes. This means that the effect introduced by the correction is translated into changing the intercept of the best fit line of Figure 4.a but keeping the slope mostly unchanged. The observed negative correlation between k_{18} and wind speed is robust, regardless of the correction implemented.

5.3 Suggested *k* values and limitations of the approach

The large footprint difference for the two inlets is the highest source of uncertainty and the limitation in our experimental setup, even with the strict filtering criteria applied to the dataset. The good agreement of our results with previous studies of the evaporation flux isotopic composition and the expected k_2/k_{18} ratio in the expected range cannot serve as validation of our method, but they provide a constraint on identifying the highest uncertainty source. As outlined in section 5.2, we identified SST differences in the footprint areas to be the main driver for the systematic bias observed for k_2. Given that SST correction does not affect k_{18} significantly, we suggest using the mean value of k_{18}=5.2‰ and k_2=4.3‰. Indeed, these k values are estimated using all the observations that maximized the validity of KP method assumptions and thus should be representative for the average conditions. When simulating ocean evaporation in isotope-

enabled General Circulation Models, k_{18} can be calculated from the 10-m wind speed using the empirical linear relationship (equation 2) and k_2 can be estimated by the average observed ratio of k_2/k_{18}=0.83. These values are valid for wind speed between 0.5 and 10 m s^{-1}.

5.4 D-excess sensitivity to evaporative conditions using suggested *k* values

Assuming that the water vapor d-excess signal is only modulated by local evaporation, the suggested non-equilibrium fractionation factors of this study can be used to predict water vapor d-excess [‰] using h_s [%] and the CA. Table 4 reports the regression coefficients (slope and intercept) of the observed and modeled d-excess vs h_s relationship using the data of this study and the data of four research cruises (Benetti et al., 2017b) which crossed the Atlantic Ocean between 2012 and 2015 at different latitudes (plots of d-excess vs h_s reported in Figure S3 and Figure S7 of Supporting Information). For computation of d-excess under CA, ocean $\delta^{18}O$ was obtained from the LeGrande and Schmidt (2006) gridded dataset, by averaging the closest 4 grid points of the ship location for each cruise, and ocean δD was estimated from the $\delta^{18}O$ vs δD relationships (Benetti et al. 2017a). The slope of the modeled d-excess vs h_s relationship is fully comparable with the one calculated for STRASSE cruise only. In general, the MAE and RMSE increase as a function of the latitude for cruises, with negligible errors for PIRATA and STRASSE. When screening the Bermuda dataset as shown in Section 3.2, the CA yields smaller regression coefficients in absolute values (-0.46 ‰/% and 46 ‰ for slope and intercept, respectively). A further decrease can be observed when the dataset is screened also by removing observations with MBL height e.g. larger than 1000 m (-0.39 ‰/% and 40‰). Given that regression coefficients for Bermuda tend to agree with the one predicted under the CA and that the STRASSE cruise was characterized by shallow boundary layer (Benetti et al., 2014), atmospheric mixing between the MBL and the free atmosphere can be one of the processes causing the discrepancy between observed d-excess variability in the MBL and the CA. Indeed, such a process (i) promotes the variability of the isotopic composition of water vapor in the free atmosphere and (ii) modulates h_s in the MBL at the same time (Benetti et al., 2018; Risi et al., 2019). Although an input of water vapor from the free atmosphere violates assumption #3 in the KP method to calculate δ_E (see section 2.5), we do not observe a significant change in estimation of δ_E and k values when screening also for MBL height ($\delta^{18}O_E$ = -3.08‰ and δD_E = - 23.06‰; k_{18} = 5.16‰ and k_2 = 4.08‰). A regression model based on observed d-excess, CA and MBL height is able to reproduce 82% of the d-excess signal variability in the entire Bermuda dataset, showing that the 55% of variability can be attributed to h_s variability and 22% to MBL height variability. Although this simplified analysis considers h_s and the height of the MBL as two independent quantities, even though they are correlated, it shows that d-excess signal in MBL water vapor might contain more information than evaporative conditions over the ocean surface. We therefore expect this study to highlight the need for more research effort to determine the processes driving d-excess signal in the MBL at the daily – subdaily scale.

6 Conclusions

Profile observations of water vapor isotopic composition near the ocean surface can be used to quantify the impact of non-equilibrium effects on isotopic fractionation during oceanic evaporation. In this study we provided a unique dataset of water vapor isotope observations collected at two different heights on a meteorological tower in Bermuda, located in the North Atlantic Ocean. Using the combination of the Keeling Plot method and the Craig-Gordon model

we have calculated the non-equilibrium fractionation factors for $^{18}O/^{16}O$ and D/H during ocean evaporation and investigated their dependency on wind speed. A strict data filtering approach was used to maximize the validity of the assumptions behind the Keeling Plot method, ensuring a robust estimate of the non-equilibrium fractionation factors. The observed non-equilibrium fractionation factor for $^{18}O/^{16}O$ is in good agreement with the established smooth wind speed parametrization in Merlivat and Jouzel (1979) (mean ± 1 std. dev k_{18}=5.2 ± 0.6‰). We find a statistically significant correlation between k_{18} and 10-m wind speed, with a sensitivity in the order of -0.16 to -0.20 ‰ m^{-1} s. Such low sensitivity would be nearly impossible to resolve by conventional measurements of the isotopic composition of water vapor at a single height above the ocean surface. Although the number of observations in high wind speed conditions is sparse in the observational dataset, the observed relationship between k_{18} and wind speed does not provide a clear indication for the presence of a discontinuity between a smooth and rough surface under different wind regimes. In fact, the rough regime parametrization of k_{18} underestimates the observed fractionation factor by a factor of ~0.66. Mean non-equilibrium fractionation factor for D/H were shown to be in the range expected following Merlivat and Jouzel (1979) albeit with a larger uncertainty (mean ± 1 std. dev k_2=4.3 ± 3.4‰). We showed that the spatial inhomogeneity of SST and ocean isotopic composition around the study site have an impact on the estimation of k_2 and its uncertainty because of the large height difference between the two inlets and the resulting different fetch areas. The results for k_{18} are robust regardless of different data filtering and are insensitive to footprint correction based on the spatial variability of SST and ocean composition. Lastly, using the non-equilibrium fractionation factors of this study and the closure assumption we showed that the d-excess signal in water vapor at the daily – subdaily temporal scale over the ocean contains information on Marine Boundary Layer height in addition to SST and RH. The results of this study allow more accurate simulation of d-excess in the MBL, hence allowing observations to be used to improve the fidelity of isotope enabled numerical models when simulating ocean evaporation.

Acknowledgments

The work was supported by the Danish Council for Independent Research – Natural Sciences grant number 10-092850 and the Carlsberg Foundation, and the AXA Research Fund. The Tudor Hill Marine Atmospheric Observatory in Bermuda was supported by NSF award OCE1829686. We acknowledge an infrastructure grant (nr. 10/0244) from the Icelandic Research Council (Rannis), that partly covered the cost of the Picarro facilities in Bermuda. HCSL and DZ acknowledges funding from the European Union's Horizon 2020 research and innovation programme under grant agreement no. 821868. H.S. acknowledges support by the Norwegian Research Council (Project SNOWPACE, grant no. 262710) and by the European Research Council (Consolidator Grant ISLAS, project no. 773245). SW acknowledges funding from the European Research Council (ERC) under the European Union's Horizon 2020 research and innovation program: Starting Grant-SNOWISO (grant agreement 759526).

Open Research

The water vapor time series used for calculating the non-equilibrium fractionation factors in the study is available on Pangea, DOI to be minted with CC BY 4.0 (Steen-Larsen et al., 2022). Code for data analysis and for reproducing plots in the article is available here: https://doi.org/10.5281/zenodo.6977090.

References

Aemisegger, F., Pfahl, S., Sodemann, H., Lehner, I., Seneviratne, S. I., & Wernli, H. (2014). Deuterium excess as a proxy for continental moisture recycling and plant transpiration. *Atmospheric Chemistry and Physics*, *14*(8), 4029–4054. https://doi.org/10.5194/acp-14-4029-2014

Aemisegger, F., & Sjolte, J. (2018). A climatology of strong large-scale ocean evaporation events. Part II: Relevance for the deuterium excess signature of the evaporation flux. *Journal of Climate*, *31*(18), 7313–7336. https://doi.org/10.1175/JCLI-D-17-0592.1

Andreas, E. L., Edson, J. B., Monahan, E. C., Rouault, M. P., & Smith, S. D. (1995). The spray contribution to net evaporation from the sea: A review of recent progress. *Boundary-Layer Meteorology*, *72*(1–2), 3–52. https://doi.org/10.1007/BF00712389

Benetti, M., Reverdin, G., Pierre, C., Merlivat, L., Risi, C., Steen-larsen, H. C., & Vimeux, F. (2014). Deuterium excess in marine water vapor: Dependency on relative humidity and surface wind speed during evaporation. *Journal of Geophysical Research: Atmospheres*, *119,* 584–593. https://doi.org/10.1002/2013JD020535

Benetti, M., Reverdin, G., Aloisi, G., & Sveinbjörnsdóttir, Á. (2017a). Stable isotopes in surface waters of the A tlantic Ocean: Indicators of ocean-atmosphere water fluxes and oceanic mixing processes. *Journal of Geophysical Research: Oceans*, *122*(6), 4723–4742. https://doi.org/10.1002/2017JC012712

Benetti, M., Steen-Larsen, H. C., Reverdin, G., Sveinbjörnsdóttir, Á. E., Aloisi, G., Berkelhammer, M. B., et al. (2017b). Data Descriptor: Stable isotopes in the atmospheric marine boundary layer water vapour over the Atlantic Ocean, 2012-2015. *Scientific Data*, *4*, 1–17. https://doi.org/10.1038/sdata.2016.128

Benetti, M., Lacour, J. L., Sveinbjörnsdóttir, A. E., Aloisi, G., Reverdin, G., Risi, C., et al. (2018). A Framework to Study Mixing Processes in the Marine Boundary Layer Using Water Vapor Isotope Measurements. *Geophysical Research Letters*, *45*(5), 2524–2532. https://doi.org/10.1002/2018GL077167

BIOS. (2021). Bermuda Atlantic Time-series Study (BATS). http://bats.bios.edu/ (Last accessed on: 14/05/2021).

Bonne, J. L., Behrens, M., Meyer, H., Kipfstuhl, S., Rabe, B., Schönicke, L., et al. (2019). Resolving the controls of water vapour isotopes in the Atlantic sector. *Nature Communications*, *10*(1), 1–10. https://doi.org/10.1038/s41467-019-09242-6

Braden-Behrens, J., Markwitz, C., & Knohl, A. (2019). Eddy covariance measurements of the dual-isotope composition of evapotranspiration. *Agricultural and Forest Meteorology*, *269–270*(January), 203–219. https://doi.org/10.1016/j.agrformet.2019.01.035

Brutsaert, W. (1965). A model for evaporation as a molecular diffusion process into a turbulent atmosphere. *Journal of Geophysical Research*, *70*(20), 5017–5024. https://doi.org/10.1029/jz070i020p05017

Brutsaert, W. (1975). A theory for local evaporation (or heat transfer) from rough and smooth surfaces at ground level. Water Resources Research, 11(4), 543–550. https://doi.org/10.1029/WR011i004p00543

Ciais, P., & Jouzel, J. (1994). Deuterium and oxygen 18 in precipitation: isotopic model, including mixed cloud processes. *Journal of Geophysical Research*, *99*(D8). https://doi.org/10.1029/94jd00412

669 Craig, H. (1961). Isotopic variations in meteoric waters. *Science*, *133*(3465), 1702–1703.
670 https://doi.org/10.1126/science.133.3465.1702
671 Craig, H., & Gordon, L. I. (1965). *Stable Isotopes in Oceanographic Studies and*
672 *paleotemperatures*. Lischi e Figli, Pisa 122.
673 Dansgaard, W. (1964). Stable isotopes in precipitation. *Tellus*, *16*(4), 436–468.
674 https://doi.org/10.3402/tellusa.v16i4.8993
675 Dee, D. P., Uppala, S. M., Simmons, A. J., Berrisford, P., Poli, P., Kobayashi, S., et al. (2011).
676 The ERA-Interim reanalysis: Configuration and performance of the data assimilation
677 system. *Quarterly Journal of the Royal Meteorological Society*, *137*(656), 553–597.
678 https://doi.org/10.1002/qj.828
679 ECMWF (2017), IFS Documentation CY43R3 - Part IV: Physical processes.
680 http://dx.doi.org/10.21957/efyk72kl
681 Galewsky, J., Steen-Larsen, H. C., Field, R. D., Worden, J., Risi, C., & Schneider, M. (2016).
682 Stable isotopes in atmospheric water vapor and applications to the hydrologic cycle.
683 *Reviews of Geophysics*, *54*(4), 809–865. https://doi.org/10.1002/2015RG000512
684 Galewsky, J., Jensen, M. P., & Delp, J. (2022). Marine Boundary Layer Decoupling and the
685 Stable Isotopic Composition of Water Vapor. *Journal of Geophysical Research:*
686 *Atmospheres*, *127*(3), 1–14. https://doi.org/10.1029/2021jd035470
687 Gat, J. R. (1996). Oxygen and Hydrogen Isotopes in the Hydrologic Cycle. *Annual Review of*
688 *Earth and Planetary Sciences*, *24*(1), 225–262.
689 https://doi.org/10.1146/annurev.earth.24.1.225
690 Gat, J. R., Klein, B., Kushnir, Y., Roether, W., Wernli, H., Yam, R., & Shemesh, A. (2003).
691 Isotope composition of air moisture over the Mediterranean Sea: An index of the air-sea
692 interaction pattern. *Tellus, Series B: Chemical and Physical Meteorology*, *55*(5), 953–965.
693 https://doi.org/10.3402/tellusb.v55i5.16395
694 Geernaert, G. L. (2003). Boundary Layers | Surface Layer. *Encyclopedia of Atmospheric*
695 *Sciences*, (1988), 305–311. https://doi.org/10.1016/b0-12-227090-8/00092-0
696 Gonfiantini, R., Wassenaar, L. I., & Araguas-Araguas, L. J. (2020). Stable isotope fractionations
697 in the evaporation of water: The wind effect. *Hydrological Processes*, *34*(16), 3596–3607.
698 https://doi.org/10.1002/hyp.13804
699 Good, S. P., Soderberg, K., Wang, L., & Caylor, K. K. (2012). Uncertainties in the assessment of
700 the isotopic composition of surface fluxes: A direct comparison of techniques using laser-
701 based water vapor isotope analyzers. *Journal of Geophysical Research Atmospheres*,
702 *117*(15), 1–22. https://doi.org/10.1029/2011JD017168
703 Good, S. P., Noone, D., Kurita, N., Benetti, M., & Bowen, G. J. (2015). D/H isotope ratios in the
704 global hydrologic cycle. *Geophysical Research Letters*, *42*(12), 5042–5050.
705 https://doi.org/10.1002/2015GL064117
706 Griffis, T. J., Wood, J. D., Baker, J. M., Lee, X., Xiao, K., Chen, Z., et al. (2016). Investigating
707 the source, transport, and isotope composition of water vapor in the planetary boundary
708 layer. *Atmospheric Chemistry and Physics*, *16*(8), 5139–5157. https://doi.org/10.5194/acp-
709 16-5139-2016
710 Hellmann, R., & Harvey, A. H. (2020). First-Principles Diffusivity Ratios for Kinetic Isotope
711 Fractionation of Water in Air. *Geophysical Research Letters*, *47*(18).
712 https://doi.org/10.1029/2020GL089999
713 Hersbach, H., Bell, B., Berrisford, P., Hirahara, S., Horányi, A., Muñoz-Sabater, J., et al. (2020).
714 The ERA5 global reanalysis. *Quarterly Journal of the Royal Meteorological Society*,

146(730), 1999–2049. https://doi.org/10.1002/qj.3803

Hijmans, R. J. (2015). Boundary, Bermuda, 2015. https://maps.princeton.edu/catalog/stanford-nw036zp7611 (Last accessed on: 14/05/2021).

Horita, J., & Wesolowski, D. J. (1994). Liquid-vapor fractionation of oxygen and hydrogen isotopes of water from the freezing to the critical temperature. *Geochimica et Cosmochimica Acta*, *58*(16), 3425–3437. https://doi.org/10.1016/0016-7037(94)90096-5

Horita, J., Rozanski, K., & Cohen, S. (2008). Isotope effects in the evaporation of water: A status report of the Craig-Gordon model. *Isotopes in Environmental and Health Studies*, *44*(1), 23–49. https://doi.org/10.1080/10256010801887174

Hu, Y., Xiao, W., Wei, Z., Welp, L. R., Wen, X., & Lee, X. (2021). Determining the Isotopic Composition of Surface Water Vapor Flux From High-Frequency Observations Using Flux-Gradient and Keeling Plot Methods. *Earth and Space Science*, *8*(3), 1–15. https://doi.org/10.1029/2020EA001304

IAEA. (2009). Reference sheet for international measurement standards - SMOW Vienna Standard Mean Ocean.

Johnsen, S. J., Dansgaard, W., & White, J. W. C. (1989). The origin of Arctic precipitation under present and glacial conditions. *Tellus, Series B*, *41 B*(4), 452–468. https://doi.org/10.3402/tellusb.v41i4.15100

Jouzel, J., Stiévenard, M., Johnsen, S. J., Landais, A., Masson-Delmotte, V., Sveinbjornsdottir, A., et al. (2007). The GRIP deuterium-excess record. *Quaternary Science Reviews*, *26*(1–2), 1–17. https://doi.org/10.1016/j.quascirev.2006.07.015

Keeling, C. D. (1958). The concentration and isotopic abundances of atmospheric carbon dioxide in rural areas. *Geochimica et Cosmochimica Acta*, *13*, 322–324. https://doi.org/10.1016/0016-7037(58)90033-4

Kljun, N., Calanca, P., Rotach, M. W., & Schmid, H. P. (2015). A simple two-dimensional parameterisation for Flux Footprint Prediction (FFP). *Geoscientific Model Development*, *8*(11), 3695–3713. https://doi.org/10.5194/gmd-8-3695-2015

Lee, X., Kim, K., & Smith, R. (2007). Temporal variations of the 18O/16O signal of the whole-canopy transpiration in a temperate forest. *Global Biogeochemical Cycles*, *21*(3), 1–12. https://doi.org/10.1029/2006GB002871

Läderach, A. and Sodemann, H., 2016: A revised picture of the atmospheric moisture residence time, *Geophysical Research. Letters*, 43, 924-933. https://doi.org/10.1002/2015GL067449

LeGrande, A. N., & Schmidt, G. A. (2006). Global gridded data set of the oxygen isotopic composition in seawater. *Geophysical Research Letters*, *33*(12), 1–5. https://doi.org/10.1029/2006GL026011

Luz, B., Barkan, E., Yam, R., & Shemesh, A. (2009). Fractionation of oxygen and hydrogen isotopes in evaporating water. *Geochimica et Cosmochimica Acta*, *73*(22), 6697–6703. https://doi.org/10.1016/j.gca.2009.08.008

Madsen, M. V., Steen-Larsen, H. C., Hörhold, M., Box, J., Berben, S. M. P., Capron, E., et al. (2019). Evidence of Isotopic Fractionation During Vapor Exchange Between the Atmosphere and the Snow Surface in Greenland. *Journal of Geophysical Research: Atmospheres*, 124(6), 2932–2945. https://doi.org/10.1029/2018JD029619

Markle, B. R., Steig, E. J., Roe, G. H., Winckler, G., & McConnell, J. R. (2018). Concomitant variability in high-latitude aerosols, water isotopes and the hydrologic cycle. *Nature Geoscience*, *11*(11), 853–859. https://doi.org/10.1038/s41561-018-0210-9

Merlivat, L., & Coantic, M. (1975). Study of mass transfer at the air-water interface by an

761 isotopic method. *Journal of Geophysical Research*, *80*(24), 3455–3464.
762 https://doi.org/10.1029/jc080i024p03455
763 Merlivat, L. (1978). Molecular diffusivities of H216O, HD16O, and H218O in gases. *The*
764 *Journal of Chemical Physics*, *69*(6), 2864–2871. https://doi.org/10.1063/1.436884
765 Merlivat, L., & Jouzel, J. (1979). Global climatic interpretation of the deuterium-oxygen 18
766 relationship for precipitation. *Journal of Geophysical Research: Oceans*, *84*(C8), 5029–
767 5033. https://doi.org/10.1029/JC084iC08p05029
768 NOAA. (2019). Bermuda 1 arc-second Coastal Digital Elevation Model.
769 https://www.ncei.noaa.gov/metadata/geoportal/rest/metadata/item/gov.noaa.ngdc.mgg.dem
770 :5010/html (Last accessed on: 14/05/2021).
771 Osman, M. B., Smith, B. E., Trusel, L. D., Das, S. B., McConnell, J. R., Chellman, N., et al.
772 (2021). Abrupt Common Era hydroclimate shifts drive west Greenland ice cap change.
773 *Nature Geoscience*, *14*(10), 756–761. https://doi.org/10.1038/s41561-021-00818-w
774 Pfahl, S., & Sodemann, H. (2014). What controls deuterium excess in global precipitation?
775 *Climate of the Past*, *10*(2), 771–781. https://doi.org/10.5194/cp-10-771-2014
776 Pfahl, S., & Wernli, H. (2009). Lagrangian simulations of stable isotopes in water vapor: An
777 evaluation of nonequilibrium fractionation in the Craig-Gordon model. *Journal of*
778 *Geophysical Research Atmospheres*, *114*(D20), 1–12.
779 https://doi.org/10.1029/2009JD012054
780 Pfahl, S., & Wernli, H. (2008). Air parcel trajectory analysis of stable isotopes in water vapor in
781 the eastern Mediterranean. *Journal of Geophysical Research Atmospheres*, *113*(D20), 1–
782 16. https://doi.org/10.1029/2008JD009839
783 Risi, C., Noone, D., Frankenberg, C., & Worden, J. (2013). Role of continental recycling in
784 intraseasonal variations of continental moisture as deduced from model simulations and
785 water vapor isotopic measurements. *Water Resources Research*, *49*(7), 4136–4156.
786 https://doi.org/10.1002/wrcr.20312
787 Risi, C., Galewsky, J., Reverdin, G., & Brient, F. (2019). Controls on the water vapor isotopic
788 composition near the surface of tropical oceans and role of boundary layer mixing
789 processes. *Atmospheric Chemistry and Physics*, *19*(19), 12235–12260.
790 https://doi.org/10.5194/acp-19-12235-2019
791 Rozanski, K., Araguás-Araguás, L., & Gonfiantini, R. (1993). Isotopic Patterns in Modern
792 Global Precipitation. *Geophysical Monograph*, *78*, 1–36.
793 https://doi.org/10.1029/gm078p0001
794 Sodemann, H., Schwierz, C., & Wernli, H. (2008). Interannual variability of Greenland winter
795 precipitation sources: Lagrangian moisture diagnostic and North Atlantic Oscillation
796 influence. *Journal of Geophysical Research Atmospheres*, *113*(3), 1–17.
797 https://doi.org/10.1029/2007JD008503
798 Steen-Larsen, H. C., Masson-Delmotte, V., Sjolte, J., Johnsen, S. J., Vinther, B. M., Bréon, F.
799 M., et al. (2011). Understanding the climatic signal in the water stable isotope records from
800 the NEEM shallow firn/ice cores in northwest Greenland. *Journal of Geophysical*
801 *Research Atmospheres*, *116*(6), 1–20. https://doi.org/10.1029/2010JD014311
802 Steen-Larsen, H. C., Sveinbjörnsdottir, A. E., Peters, A. J., Masson-Delmotte, V., Guishard, M.
803 P., Hsiao, G., et al. (2014). Climatic controls on water vapor deuterium excess in the
804 marine boundary layer of the North Atlantic based on 500 days of in situ, continuous
805 measurements. *Atmospheric Chemistry and Physics*, *14*(15), 7741–7756.
806 https://doi.org/10.5194/acp-14-7741-2014

Steen-Larsen, H. C., Sveinbjörnsdottir, A. E., Jonsson, T., Ritter, F., Bonne, J. -L., Masson-Delmotte, V., et al. (2015). Moisture sources and synoptic to seasonal variability of North Atlantic water vapor isotopic composition. *Journal of Geophysical Research Atmospheres*, *120*. https://doi.org/10.1002/2015JD023234

Steen-Larsen, H. C., Peters, A. J., Wahl, Sveinbjörnsdóttir, Á. E., Zannoni, D. (2022). Calibrated stable water vapor isotope data at 2.5 m ASL and 50 m ASL from Tudor Hill Marine Atmospheric Observatory, Bermuda. *PANGAEA*, [Dataset] https://doi.org/10.1594/PANGAEA.949607

Stewart, M. K. (1975). Stable isotope fractionation due to evaporation and isotopic exchange of falling waterdrops: Applications to atmospheric processes and evaporation of lakes. *Journal of Geophysical Research*, *80*(9), 1133–1146. https://doi.org/10.1029/jc080i009p01133

Stull, R. B. (1997). *An Introduction to Boundary Layer Meteorology*. Springer.

Thurnherr, I., Kozachek, A., Graf, P., Weng, Y., Bolshiyanov, D., Landwehr, S., et al. (2020). Meridional and vertical variations of the water vapour isotopic composition in the marine boundary layer over the Atlantic and Southern Ocean. *Atmospheric Chemistry and Physics*, *20*(9), 5811–5835. https://doi.org/10.5194/acp-20-5811-2020

Thurnherr, I., Hartmuth, K., Jansing, L., Gehring, J., Boettcher, M., Gorodetskaya, I., et al. (2021). The role of air–sea fluxes for the water vapour isotope signals in the cold and warm sectors of extratropical cyclones over the Southern Ocean. *Weather and Climate Dynamics*, *2*(2), 331–357. https://doi.org/10.5194/wcd-2-331-2021

Uemura, R., Matsui, Y., Yoshimura, K., Motoyama, H., & Yoshida, N. (2008). Evidence of deuterium excess in water vapor as an indicator of ocean surface conditions. *Journal of Geophysical Research Atmospheres*, *113*(19), 1–10. https://doi.org/10.1029/2008JD010209

Uemura, R., Barkan, E., Abe, O., & Luz, B. (2010). Triple isotope composition of oxygen in atmospheric water vapor. *Geophysical Research Letters*, *37*(4), 1–4. https://doi.org/10.1029/2009GL041960

UK MET OFFICE. (2005). OSTIA L4 SST Analysis. Ver. 1.0. PO.DAAC. https://doi.org/https://doi.org/10.5067/GHOST-4FK01

Veron, F. (2015). Ocean spray. *Annual Review of Fluid Mechanics*, *47*, 507–538. https://doi.org/10.1146/annurev-fluid-010814-014651

Wahl, S., Steen-Larsen, H. C., Reuder, J., & Hörhold, M. (2021). Quantifying the Stable Water Isotopologue Exchange Between the Snow Surface and Lower Atmosphere by Direct Flux Measurements. *Journal of Geophysical Research Atmospheres*, *126*(13), 1–24. https://doi.org/10.1029/2020JD034400

Yakir, D., & Wang, X. F. (1996). Fluxes of CO2 and water between terrestrial vegetation and the atmosphere estimated from isotope measurements. *Nature*, *380*(6574), 515–517. https://doi.org/10.1038/380515a0

Zannoni, D. (2022). Bermuda-NEFF, Release of code to calculate non-equilibrium fractionation factors after first cycle of peer review. [Software] https://doi.org/10.5281/zenodo.6977090

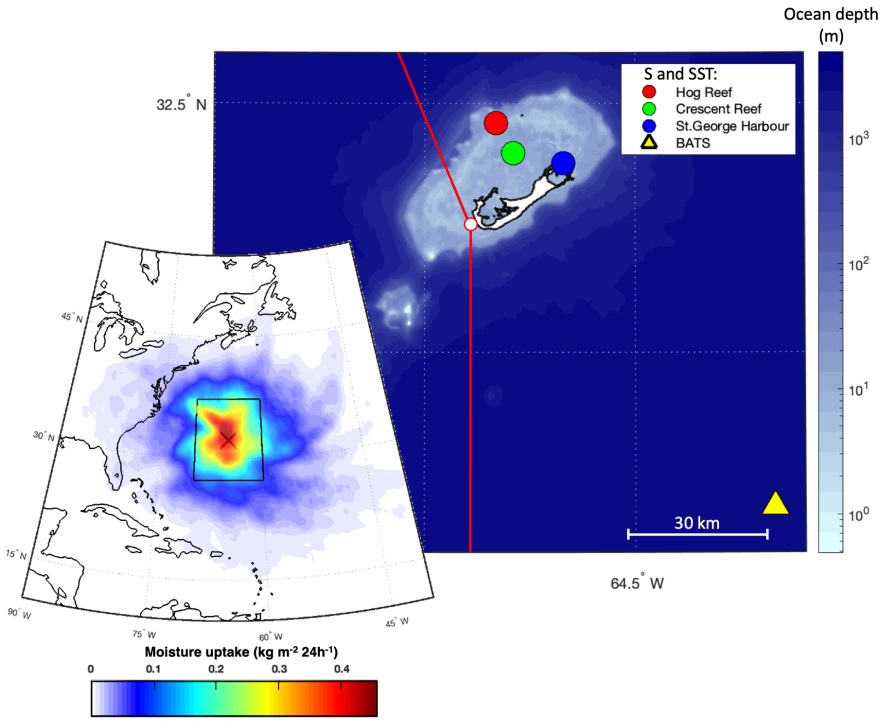

Figure 1: Study site in Bermuda. Bermuda Island shape in white color and ocean depth as color scale (Hijmans, 2015; NOAA, 2019): position of Tudor Hill Marine Atmospheric Observatory (white dot) and wind sector (red lines) to discriminate local transpired water vapor from ocean water vapor (N180˚ to N340˚). Colored circles and triangle are the sampling locations of available salinity (S) and SST time series around the study area. The large-scale map on the left shows the location of Bermuda (cross) in the northwest Atlantic Ocean and the main water vapor sources during the study period. The highlighted sector includes 45% of accounted water vapor uptakes.

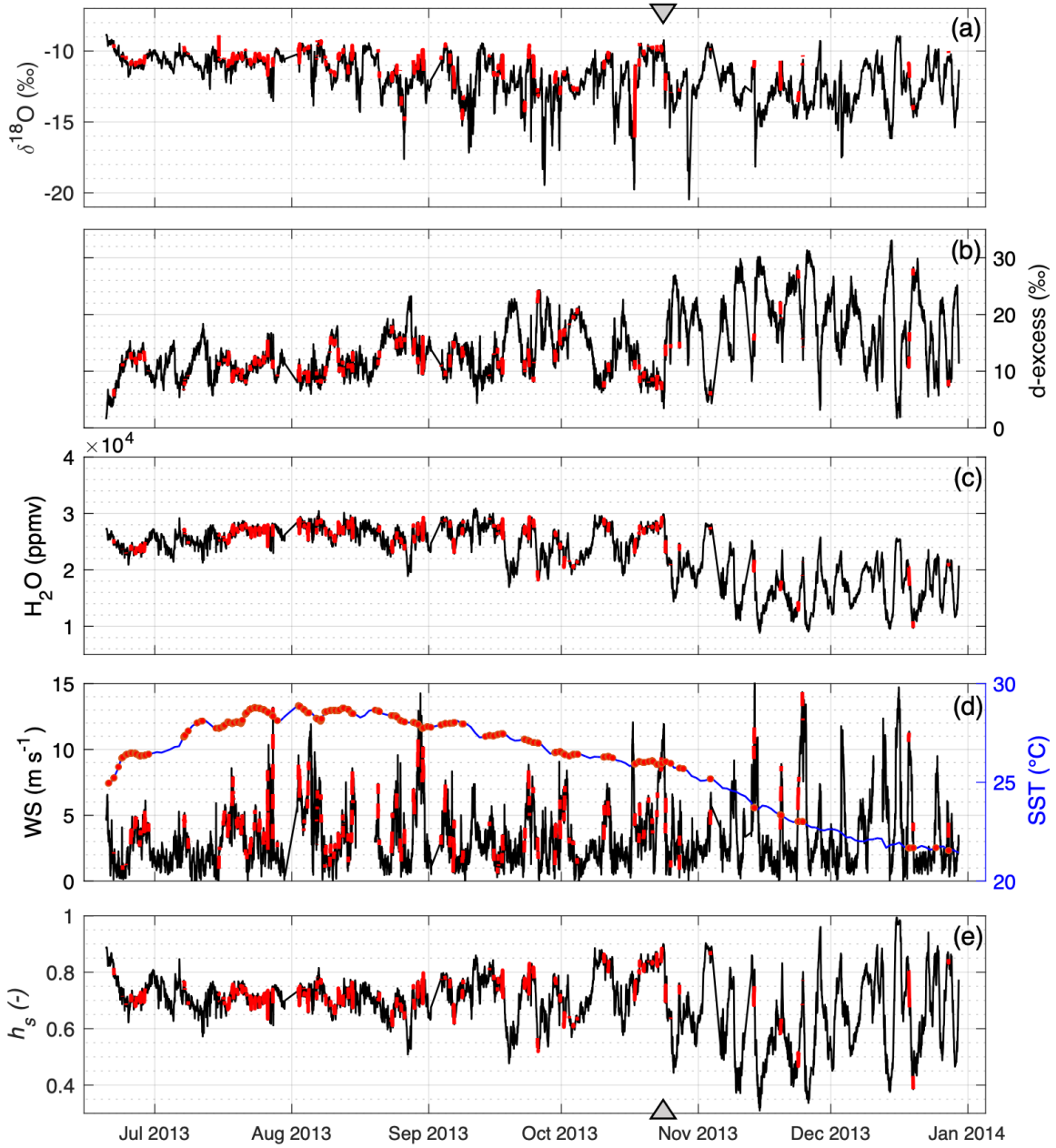

Figure 2: Timeseries of water vapor isotopic composition and relevant meteorological parameters at the study site. **(a, b)** Water vapor isotopic composition, **(c)** mixing ratio and **(d)** wind speed (WS) measured at top inlet height (50 m AMSL). SST data from OSTIA reported as a blue line. **(e)** h_s is the relative humidity measured at top inlet and normalized to OSTIA SST. Gray triangles on the top and bottom of the figure represent the autumn transition, as detected from d-excess variability at weekly scale. Observations selected for estimating the isotopic composition of the evaporation flux are highlighted in red.

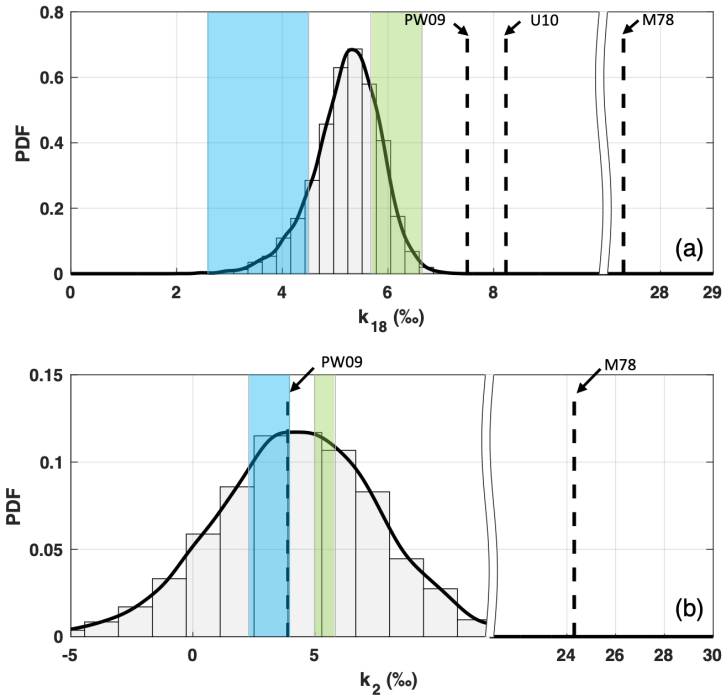

Figure 3: Non-equilibrium fractionation factors estimated from flux observations (KP method). Continuous kernel density function was estimated with bandwidths 0.1‰ and 0.6‰ for k_{18} **(a)** and k_2 **(b)**, respectively. Shaded area represents the k intervals predicted for smooth (green, 10-m wind speed range [1-6] m s^{-1}) and rough (cyan, 10-m wind speed range [6-13] m s^{-1}) regimes following Merlivat and Jouzel (1979). For reference, molecular diffusivity ratios M78 (Merlivat, 1978) and non-equilibrium fractionation factors for ocean settings PW09 (Pfahl & Wernli, 2009) and U10 (Uemura et al., 2010) are reported as vertical dashed lines.

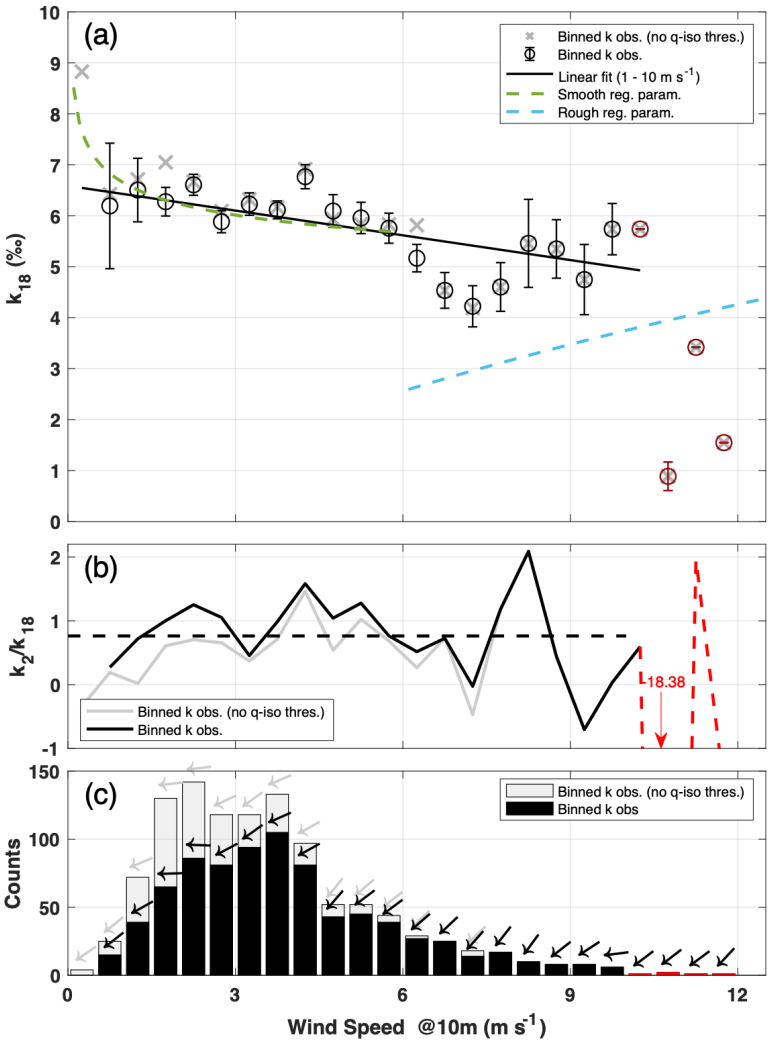

871
872 **Figure 4:** Observed relationship between k_{18} and 10-m wind speed. **(a)** mean ± standard error of k_{18} estimated for
873 each wind speed class. Green and cyan lines show the parametrization of k_{18} for smooth and rough wind regimes,
874 respectively (Merlivat & Jouzel, 1979). Solid black line represents a linear fit (R^2=0.52) in the wind speed interval
875 0.5 – 10 m s^{-1} (fit equation reported in text). **(b)** k_2/k_{18} ratio for each wind speed class. Dashed black line is the
876 average ratio (0.8). **(c)** Number of observations and mean wind direction (arrows) for each bin. In all panels: black
877 lines, black symbols and black bars for filtered dataset; gray lines, gray symbols and gray bars for filtered dataset
878 with no isotope and humidity thresholds implemented (Table 1, rows 3 and 4): red line, red symbols and red bars
879 highlight wind speed classes with number of observations ≤ 2.
880

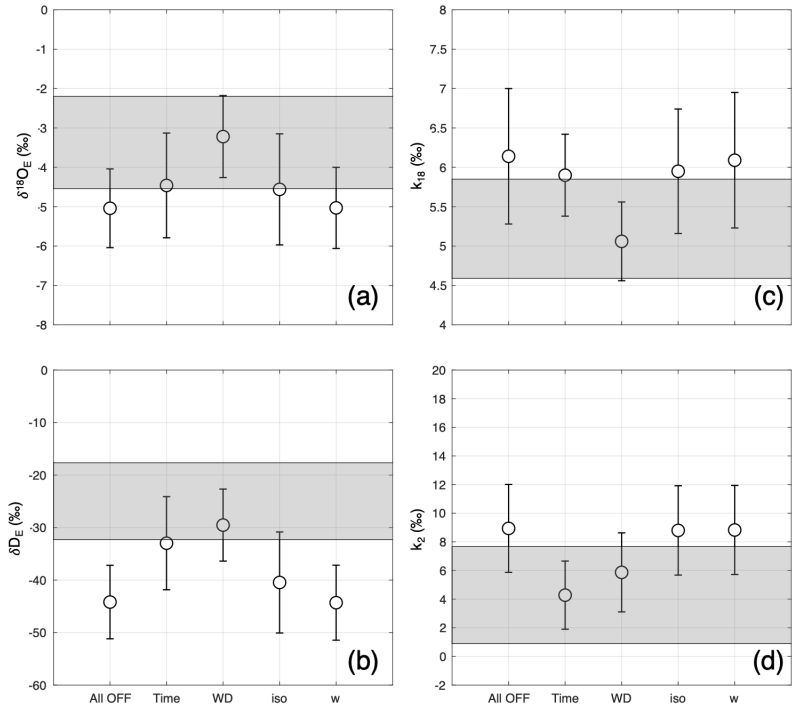

Figure 5: Sensitivity of the method for estimating δ_E and k values to filtering criteria. Following Table 1: only precipitation filter (All off, n = 6834), time + precipitation filter (Time, n = 2016), wind sector + precipitation (WD, n = 3143), isotopic gradient + precipitation (iso, n = 3883), humidity gradient+ precipitation (w, n = 6484). **(a)** and **(b)** sensitivity of isotopic composition of evaporation flux (δ_E) for $\delta^{18}O$ and δD, respectively. **(c)** and **(d)** sensitivity of non-equilibrium fractionation factors for k_{18} and k_2, respectively. For all panels, gray shaded areas represent mean ± 1 std. deviation when enabling all filtering steps.

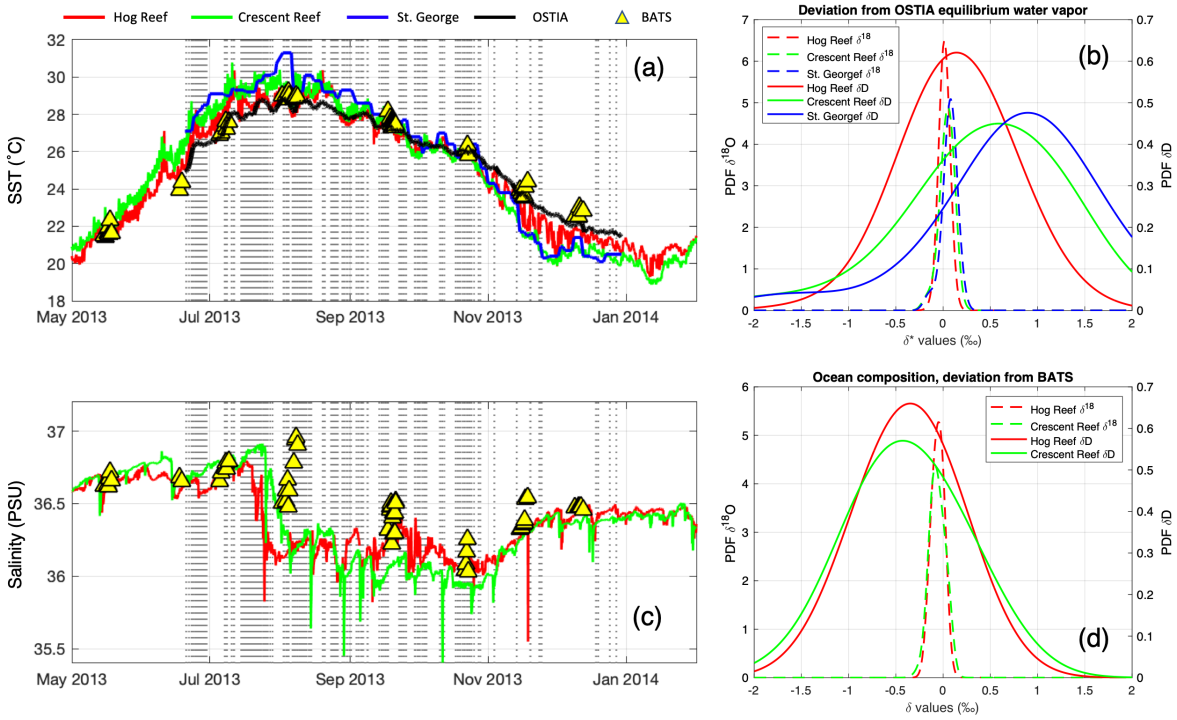

Figure 6: SST and salinity inhomogeneity of ocean waters around the study site. **(a)** Time series of SST in different points of the study area, see Figure 1 for reference of sampling sites. Vertical lines represent selected observations for flux estimation. **(b)** PDFs of $\delta^{18}O$ and δD [Equilibrium vapor (SST reef) – Equilibrium vapor (SST OSTIA)], where SST reef is the SST measured in different points within the reef area. **(c)** Similar to (a) but for salinity. **(d)** PDFs of $\delta^{18}O$ and δD [Ocean Composition (S reef) – Ocean Composition (S BATS)], where S reef is the salinity measured at different points within the reef area and S BATS is salinity measured at the BATS site. Conversion of salinity to isotopic composition following Benetti et al. (2017a).

898 **Table 1:** List of variables and constraints adopted to filter the time series.

Variable	Indexing	Range/Value	Rejected (cumulative)	Assumption #	Rationale
Time	Time	Daytime observations based on sunrise-sunset hour (LST) with 2 hours symmetrical offset	71%	2,4	No influence of dew formation caused by night cooling
WD	Wind sector inclusion	Western Sector 180°N – 340°N (i.e. excluding winds from inland)	85%	3,4	No influence of local evapotranspiration from vegetation
δD and $\delta^{18}O$	$\lvert\delta D_{Bottom}-\delta D_{Top}\rvert$ $\lvert\delta^{18}O_{Bottom}-\delta^{18}O_{Top}\rvert$	> 1 ‰ > 0.1 ‰	89%	2	Difference between Top/Bottom larger than instrumental precision (L2120-i)
w	$w_{Bottom} - w_{Top}$	> 100 ppmv*	89%	2	w decreases with height above ocean
P	Time	No precipitation within the last two hours	90%	1,2,3,4	No vapor recycling from precipitation

899
900 The column "rejected" reports the size of dataset that does not fulfill each filtering threshold. Assumption n# refers
901 to the numbered list in Section 2.5. * This is a conservative estimate of instrumental precision not reported in the
902 L2120-i datasheet.
903

904 **Table 2:** Descriptive statistics of evaporation flux and top inlet water vapor isotopic composition at the daily
905 timescale. Interquartile range (IQR) estimated by fitting a normal PDF on observed δ_E distribution. $\sigma_{\delta E}$ following
906 Good et al., (2012).

	Mean (‰)	Median (‰)	IQR (‰)	$\sigma_{\delta E}$ (‰)
Evaporation flux $\delta^{18}O$	-3.37	-4.48	-6.7 ; -0.04	1.17
Evaporation flux δD	-24.99	-33.48	-48.38 ; -1.60	7.33
Top inlet water vapor $\delta^{18}O$	-11.30	-10.97	-12.10 ; -10.51	-
Top inlet water vapor δD	-78.13	-76.14	-83.15 ; -73.10	-

907

908 **Table 3:** Impact of SST and Ocean composition variability on k_2, k_{18} and on k_{18} vs wind speed parameters
909 estimation. Uncertainties are: 0.6‰, 3.5‰, 0.04 and 0.3 for k_{18}, k_2, slope and intercept, respectively. Deviations
910 from *k* values obtained without applying any correction.

Correction	**Cause**	***k*$_{18}$ (‰)**	**Dev. (%)**	***k*$_2$ (‰)**	**Dev. (%)**	***k*$_2$/*k*$_{18}$**	**Slope (‰ m^{-1} s)**	**Interc. (‰)**
No correction	-	6.0	-	12.74	-	2.11	-0.20	7.93
Salinity correction	Different isotopic composition of surface water in fetch area	5.8	-4	11.37	-11	1.96	-0.21	7.72
SST correction	SST inhomogeneity in fetch area	5.2	-14	4.32	-66	0.83	-0.16	6.59
Salinity + SST corrections	SST and surface composition inhomogeneity	5.0	-18	2.81	-78	0.57	-0.17	6.37

911

912 **Table 4:** D-excess [‰] vs h_s [%] relationship: observed and modeled under CA. Observations from ACTIV, RARA,
913 STRASSE and PIRATA cruises averaged over 15 min (Benetti et al. 2017b). Slopes and intercepts reported with
914 their (± standard error). For modeled d-excess, standard error of the slope is always <0.01. Mean Absolute Error
915 (MAE) and Root Means Squared Error (RMSE) of observed d-excess vs modeled d-excess (CA).

Dataset	**SST source**	**Observed d-excess**		**Modeled d-excess**		**MAE (‰)**	**RMSE (‰)**
		Slope *(‰/%)*	**Interc. (‰)**	**Slope *(‰/%)***	**Interc. (‰)**		
ACTIV (n = 3087)	OSTIA (200 km x 200 km)	-0.32 (± 0.01)	33.71 (± 0.46)	-0.40	34.43 (± 0.07)	6.52	3.47
RARA (n = 5115)	On board SBE38 (1.50 m depth)	-0.38 (<0.01)	39.58 (± 0.20)	-0.43	41.58 (± 0.23)	2.60	2.46
STRASSE (n = 2224)	On board SBE35 (3.50 m depth)	-0.38 (± 0.01)	38.35 (± 0.40)	-0.38	38.51 (± 0.12)	1.12	1.44
PIRATA (n = 2662)	On board SBE3S (3.33 m depth)	-0.24 (± 0.01)	29.37 (± 0.47)	-0.41	40.83 (± 0.18)	0.89	0.93
Bermuda this study (n = 8791)	OSTIA (1˚x1˚)	-0.48 (<0.01)	47.91 (± 0.16)	-0.36	35.48 (± 0.04)	3.82	4.46

916